PAPER

Check for updates

Charge pattern affects the structure and dynamics of polyampholyte condensates†

Milan Kumar Hazra and Yaakov Levy ⓘD *

Proteins with intrinsically disordered regions have a tendency to condense *via* liquid–liquid phase separation both *in vitro* and *in vivo*. Such biomolecular coacervates play various significant roles in biologically important regulatory processes. The present work explores the structural and dynamic features of coacervates formed by model polyampholytes, being intrinsically disordered proteins, that differ in terms of their charged amino acid patterns. Differences in the distribution of charged amino acids along the polyampholyte sequence lead to distinctly different structural features in the dense phase and hence to different liquid properties. Increased charge clustering raises the critical temperature for phase separation and results in each polyampholyte experiencing a larger number of inter-chain contacts with neighboring proteins in the condensate. Consequently, polyampholytes with greater charge clustering adopt a much more extended conformation, having a radius of gyration up to twice that observed in the dilute bulk phase. Translational diffusion within the droplet is pronounced, being just 4–20 times slower than in the bulk, consistently with the high conformational entropy in the dense phase and high exchange rate of the network of intermolecular interactions in the condensate. Coupled to the faster diffusion, the condensate also adopts a more elongated shape and exhibits imperfect packing, which results in cavities. This study quantifies the fundamental microscopic properties of condensates including the effect of long-range electrostatic forces and particularly how they can be modulated by the charge pattern.

Introduction

A living cell is a complex environment containing a large number of different proteins, lipids, nucleic acids, and small molecules. The phenomenon of phase separation,[1,2] particularly liquid–liquid phase separation (LLPS)[3,4] into a condensed phase and a dilute bulk phase, enables cells to obtain spatial and temporal control over their molecular functionality and interactions by means of intracellular liquid-like membraneless organelles. Such membraneless organelles play significant roles in several cellular mechanisms, including gene expression,[5,6] cellular signaling,[7–9] regulation of protein translation,[10] and RNA transcription.[5] The organelles generally consist of the dense phase, which takes the form of polymer-rich condensate droplets referred to as coacervates. These coacervates are often enriched in intrinsically disordered proteins that exhibit several interaction motifs (or "stickers"[11–13]) that define a multivalent interaction.[3,9,14] In recent years, several studies showed that the formation and dissolution of the droplet phase can be modulated by cellular conditions, namely temperature, pH, salt

concentration,[15] and post-translational modifications such as phosphorylation.[16] Experimental studies showed that the condensate has liquid-like properties[1,2,17] and that its formation is mediated by entropy.[18] The dynamics within the condensates is supported by the extensive dynamics of the low complexity regions, which remain disordered as in dilute solution.[19–21] Picosecond time-resolved fluorescent depolarization measurements have revealed rapid large amplitude torsional fluctuations in the extended chains, with these in turn controlling the formation and breakage of inter-chain contacts, hence maintaining the fluidity of the dense phase.[22]

The molecular driving forces underlying the phase separation of proteins are diverse and include electrostatic, hydrophobic, cation–π, and π–π interactions, as well as hydrogen bonding.[23,24] In some instances, the protein condensates formed *via* LLPS are stabilized by electrostatic interactions between oppositely charged patches in the sequence (for example, the DDX4 protein[25]), whereas the driving force for the LLPS of other proteins may be governed by aromatic interactions (for example, the FUS protein[26] and prion-like domains[27]). To decipher the stability of condensates and their molecular driving forces, various experimental techniques have been applied to study the structure and internal dynamics of proteins and their mutants in solution and droplet form.

Computational studies[28–33] have joined the effort to characterize the biophysics of bimolecular condensates formed *via* LLPS.

Department of Structural Biology, Weizmann Institute of Science, Rehovot, 76100, Israel. E-mail: Koby.Levy@weizmann.ac.il; Tel: +972-8-9344587
† Electronic supplementary information (ESI) available. See DOI: 10.1039/d0cp02764b

These studies address some structural and energetic properties of model systems[31,34] or natural proteins[24,28,35] that participate in LLPS. Although condensates of several proteins and their mutants were studied computationally, the microscopic structural and dynamic features of these proteins in the dense phase are still poorly understood.

In the current study, we aim to quantify the structure and dynamics of intrinsically disordered proteins whose condensate formation is driven by long-range electrostatic interactions. We studied polyampholytes comprised of positively and negatively charged monomers and bearing zero net charge, such that they differ solely in terms of the distribution of the charges along the chain. The various degrees of clustering of like charges along the chain can be quantified by the patterning order parameter, κ.[36] κ equals unity when there is complete segregation of the positive and negative charges, whereas κ equals zero relates to maximal mixing. Such polyampholytes are model systems for intrinsically disordered proteins and their LLPS was shown to depend on charge patterning, which, in some cases, is correlated with κ.[31,32,37] Nonetheless, our study aims to quantify how long-range electrostatic interactions and its dependence on κ govern the liquid nature of the condensate. The composition and organization of the charges may affect both conformational preference and diffusion of the peptides in bulk and in the condensate.

Methods

As all-atom simulations are constrained to the early stages of LLPS and are limited to a small number of protein chains,[35,38,39] we applied a coarse-grained model that allows comprehensive analysis of the conformational heterogeneity and dynamics in the condensates. The polyampholytic intrinsically disordered proteins were modeled by a single bead for each residue that was assigned a positive or negative unit charge to produce an electrostatically neutral polymer. The potential energy function consisted of bonded, angular, electrostatic, and short-range repulsions. The bonded and angular interactions were modelled with a harmonic potential. In most of the simulations, the polymers remained completely flexible without any dihedral constraint. To examine the effect of conformational rigidity, we introduced a dihedral potential

$$\sum_{\text{dihedrals}} K_{\text{dihedrals}}\left[1 - \cos\left(\varphi_{ijkl} - \varphi^0_{ijkl}\right) - \cos\left(3\varphi_{ijkl} - \varphi^0_{ijkl}\right)\right]; \text{ where}$$

φ_{ijkl} is the dihedral angle between subsequently bonded backbone beads i–j–k–l in radians, φ^0_{ijkl} is the optimal dihedral angle between subsequently bonded backbone beads i–j–k–l in radians. The strength of the dihedral potential, $K_{\text{dihedrals}}$, was varied between 0–2. If not mentioned otherwise, the polyampholytes were modeled as flexible peptides with $K_{\text{dihedrals}} = 0$.

Electrostatic interactions among the amino acid residues were modeled by the Debye–Hückel potential, which accounts for the ionic strength:[40] $E_{\text{electrostatic}} = K_{\text{Coulomb}} B(\kappa) \sum_{i,j} \dfrac{q_i q_j e^{-\kappa r_{ij}}}{\varepsilon r_{ij}}$; q_i and q_j denotes the charge of the ith and jth bead. r_{ij} denotes

the inter-bead distance. ε is the solvent dielectric constant. $K_{\text{Coulomb}} = 4\pi\varepsilon_0 = 332$ kcal mol^{-1}. $B(\kappa)$ is dependent on salt concentration and the radius (a) of ions produced by the dissociation of the salt, $B(\kappa) = \dfrac{e^{\kappa a}}{1 + e^{\kappa a}}$. According to Debye–Hückel theory, the range of electrostatic interaction of an ion is of the order of κ^{-1} which is called the Debye screening length. Poisson–Boltzmann equation leads to the following relation of κ and ionic strength $\kappa^2 = \dfrac{8\pi N_A e^2 \rho_A I}{1000\varepsilon k_B T}$; where N_A is the Avogadro number, e is charge of an electron, ρ_A is the solvent density, I denotes the ionic strength of the medium. k_B is the Boltzmann constant and T is temperature. In addition to the electrostatics, each bead interacts with all the other beads with a repulsion potential, $E_{\text{repulsion}} = \left(\dfrac{\sigma_{ij}}{r_{ij}}\right)^{12}$ with $\sigma_{ij} = 4$ Å.

We simulated polymers consisting of either 20 or 40 residues. The condensate was studied by simulating 100 polymers placed in a box with dimensions $300 \times 300 \times 300$ Å (for 20 residue polyampholytes the box dimension was 240 Å). The structure and dynamical features of the polymers were studied at a salt concentration of 0.02 M with a dielectric constant of 80 and at temperatures below the critical temperature of the sequence of interest (we note that due to the coarse-grained representation, the used salt concentration in the simulations represents an effectively higher salt concentration). At each temperature, multiple trajectories were simulated in order to have proper averaging. A random conformation was used as each polyampholytes in the simulation box to initiate the simulation. Multiple trajectories were simulated at various temperature by solving the Langevin equation. The simulated polyampholytes were clustered at each time step to define their clustering into condensates and particularly the largest condensate.
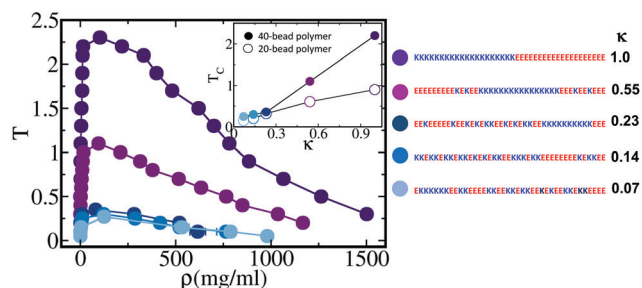

Fig. 1 Temperature–density phase diagram of model polyampholyte sequences. The phase diagram was plotted from extensive coarse-grained molecular dynamics simulations of five different sequences of 40-bead polyampholytes possessing different charge patterns. The distribution of the charges along the sequences is represented by the κ parameter. The sequences of the polyampholytes and their corresponding κ values are shown on the right. The critical temperature (T_c) was evaluated from the following relation of the universal scaling of density near the critical point, $\rho_{\text{Densephase}} - \rho_{\text{Dilutephase}} = A\left(1 - \dfrac{T}{T_c}\right)^{\beta}$. The inset shows the relationship between the critical temperature and the κ parameter for both 40- and 20-bead polyampholytes (filled and empty circles, respectively). Coloring in the plots follows the color scheme of the sequences.

Results and discussion

Sequence-dependent phase co-existence and critical point

To elucidate the temperature dependence of the stability of the droplet phase as the charge pattern changes in a sequence, we plot the temperature–density phase diagram for the designed sequences with different values of κ (Fig. 1 and Fig. S1, ESI†). To obtain the phase diagram, we used the condensate geometry to estimate the density of the dense phase. In each time frame, the density of the condensate was estimated by counting the number of polymer beads in a sphere of radius 5 nm around the center of mass (COM) of the largest cluster of interacting polymers. A clustering algorithm was used to determine the largest cluster, with an inter-chain COM distance cut-off of 3 nm. We measured the critical temperature, T_c, and density, ρ, by fitting the density–temperature data to the following relation: $\rho_{\text{Densephase}} - \rho_{\text{Dilutephase}} = A\left(1 - \dfrac{T}{T_c}\right)^{\beta}$, where $\rho_{\text{Densephase}}$ and $\rho_{\text{Dilutephase}}$ denote the polymer bead density in the dense phase and in the dilute phase, respectively, and β is a critical exponent that, following other studies, was set to 0.325.[29,34] The critical temperature rises with increasing κ. This is likely related to enrichment of charge patches, which mediate inter-chain

contacts. The inset shows the dependence of T_c on κ for two different polymer sets of length 20 or 40 beads, illustrating that higher κ is linked to greater T_c.[31,32]

Structural features of polymers in the condensate and the bulk

To understand the microscopic structural characteristics of the polymers in LLPS, we compared the distribution of the radius of gyration (R_g) for polymers in the dense phase and the bulk (Fig. 2A and Fig. S2, ESI†). Larger R_g values were calculated in the dense condensate compared with the bulk, illustrating a transition from a compact to a more extended conformation upon LLPS. The different conformational preferences of polyampholytes in the condensate and the bulk are also reflected by the Flory exponent, which is $\nu \sim 0.6$–0.7 in the dense phase and is independent of κ (at a fixed T/T_c), whereas it has a value of $\nu \sim 0.3$–0.5 in the bulk, depending upon the value of κ (Fig. S3, ESI†).

To focus on the effect of LLPS on the conformation of the polyampholytes, we followed the ratio $R_{\text{gDroplet}}/R_{\text{gBulk}}$ which is shown to depend on T/T_c and on κ and can even reach a value as large as 2 (Fig. 2B). A similar dependence of $R_{\text{gDroplet}}/R_{\text{gBulk}}$ on T/T_c is evident for both 40- and the 20-bead polymer chain systems (see Fig. S4, ESI†). The extent of the expansion of the
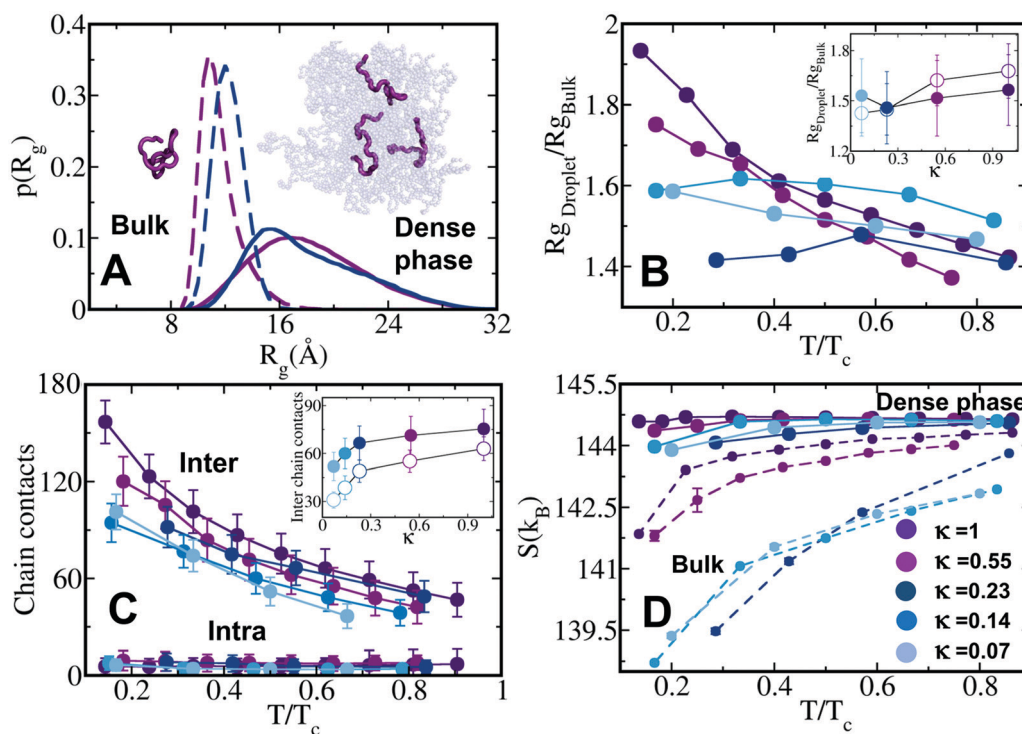

Fig. 2 Conformational preferences of polymers in the dense phase. (A) Probability distribution of the radius of gyration ($p(R_g)$) for polymers in the dense phase (solid lines) and in the bulk (dashed lines) for $\kappa = 0.55$ and $\kappa = 0.23$ at $T = 0.5T_c$. The R_g distributions in the dense phase are shifted to the right and are significantly broader than in the bulk, implying the presence of more extended conformations and large-scale conformal fluctuations in the dense phase. The inset illustrates three extended conformations adopted by the polyampholytes with $\kappa = 0.55$ at $T = 0.5T_c$ in the dense phase whereas a collapsed state is observed in bulk. (B) Ratio of average polymer R_g in the dense phase and the bulk as a function of temperature scaled with respect to the critical temperature (T/T_c) of each sequence. Inset shows the variation of the R_g ratio as a function of κ for both 40- and 20-bead polyampholytes (filled and empty circles, respectively) at $T = 0.5T_c$. (C) Average inter-chain and intra-chain contacts in the dense phase as a function of T/T_c. Inset shows the variation of inter-chain contact with κ for the two different polymer sizes. The average number of intra-chain contacts of the polymers in the bulk is shown in Fig. S7 (ESI†). (D) Conformational entropy of the polyampholytes in the dense phase (solid line) and bulk (dashed lines) measured by the flexibility of each dihedral angle in the polymers.

19370 | *Phys. Chem. Chem. Phys.*, 2020, **22**, 19368–19375

This journal is © the Owner Societies 2020

chain in the condensate depends on κ and on T. At $T = 0.5T_c$, the ratio $R_{gDroplet}/R_{gBulk}$ increases with κ, for polymer of lengths of 20 or 40 beads (see Fig. 2B inset). We note that the dependence of this ratio on κ is weak and not valid at all temperatures, suggesting limitations on the suitability of the κ parameter for capturing nuances in R_g[32] (we note that the κ values of the studied systems correlated well with their sequence charge decoration (SCD) values (Fig. S5, ESI†)[32]).

Polyampholytes with κ of 0.55 or 1.0 can adopt much more extended conformations than those with lower κ values, particularly at low temperature. A monotonic decrease in $R_{gDroplet}/R_{gBulk}$ is observed for these polyampholytes when temperature is increased. This dependence is weaker for polyampholytes with $\kappa = 0.55$ than those with $\kappa = 1.0$ and becomes even weaker for systems with κ values of 0.07–0.23. Higher T results in more expanded polymer conformations in both the bulk and the condensate, as a result of the disruption of intra-chain contacts. The origin for the decrease in $R_{gDroplet}/R_{gBulk}$ when T increases is primarily because R_{gbulk} is more sensitive to changes in T. In all the studied systems, R_g is about 40–60% more extended in the condensate than in the bulk when the temperature is ~80% of the corresponding T_c (Fig. 2B).

The origin of the stronger effect of temperature on the $R_{gDroplet}/R_{gbulk}$ ratio for polyampholytes with higher κ values than those with lower values (*i.e.*, for systems with $\kappa = 0.55$ or 1.0 *versus* $\kappa = 0.07$–0.23) may lie in differences in the stability of the condensate, which is determined by the network of interactions between the constitutive polymers. To investigate this possibility, we measured the number of intermolecular interactions formed between a polymer in the condensate and its neighboring polymers. Fig. 2C shows that the average number of intermolecular interactions of a polymer in the condensate decreases as the temperature increases for all values of κ. The extensive intermolecular interactions each polymer chain forms with its neighboring polymers in the condensate, while the number of intramolecular interactions is low and insensitive to variation in T (Fig. 2C and Fig. S6, S7, ESI†), explains the expansion of the conformation, as reflected by the R_g values (Fig. 2A and B). For a given value of T/T_c, the number of intermolecular interactions is larger for polymers with higher κ (Fig. 2C, inset). In particularly, at a very low temperature ($T/T_c \sim 0.2$), the number of intermolecular interactions for polymers with high κ (*i.e.*, $\kappa = 0.55$ and especially for $\kappa = 1.0$) is higher than for lower κ. This may suggest that these systems are more saturated with interactions with neighboring chains and the droplet is therefore denser than that formed by polymers with lower values of κ, consequently chains with $\kappa = 0.55$ or $\kappa = 1.0$ have more extended conformations in the condensate at very low temperatures. The high packing found at low T for polyampholytes with high κ values can explain their high $R_{gDroplet}/R_{gBulk}$ ratio at low T (Fig. 2B). As the system approaches criticality, the average lifetime of the inter-chain contacts also decreases (Fig. S8, ESI†).

The expansion of the polymer conformation following LLPS, as reflected by the shift in the R_g distribution, is also associated with a significant broadening of R_g distribution in the dense phase compared with a narrow R_g distribution of the polyampholytes in the bulk (Fig. 2A). Such broadening indicates that polymers in the dense phase possess greater conformational fluctuation compared with those in the bulk. To understand the
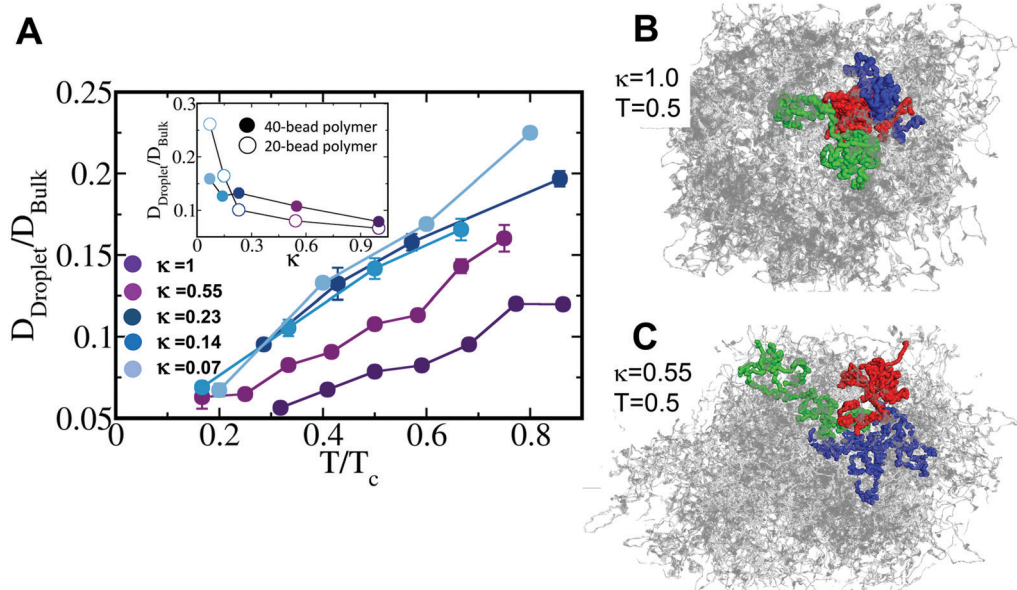

Fig. 3 Translational diffusion in the condensate. (A) The ratio of the translational diffusion coefficient (D) in the dense droplet phase to the bulk is shown as a function of temperature scaled to the critical temperature (T/T_c) of each sequence. Inset shows the dependence of the diffusion coefficient ratio on κ at $T = 0.5T_c$ for both 40- and 20-bead polyampholytes (filled and empty circles, respectively). The degree of diffusion in the dense phase for different κ values is illustrated pictorially for $\kappa = 1.0$ (B) and $\kappa = 0.55$ (C), both at $T = 0.5$. These plots show projections of the center of mass of three selected chains (colored green, red, and blue) for 2000 timesteps (which correspond to ~30 times the life time of an intermolecular contact), whereas the centers of mass of the other chains in the droplet are colored grey. The plots illustrate that a decrease in κ facilitates diffusion in the dense phase.

This journal is © the Owner Societies 2020

Phys. Chem. Chem. Phys., 2020, **22**, 19368–19375 | **19371**

conformational heterogeneity in the dense phase, we calculated the conformational entropy of the dense phase compared with the bulk (Fig. 2D). Conformational entropy is estimated from variations in all the dihedral angles within the polymer, as follows, $S = \sum_{i=1}^{n_{polymer}} \sum_{j=1}^{n_{dihedral}-3} \sum_{k=-\pi}^{\pi} p_k^j \ln(p_k^j)$, where p_k^j represents the probability of the jth dihedral angle to sample the kth conformation. The conformational entropy is higher in the dense phase than in the bulk. Moreover, the conformational entropy is less sensitive to κ or to temperature in the dense phase compared with the bulk phase. This finding is well supported by the observation that the distribution of R_g in the dense phase is broad, leading to an enhanced sampling of the conformational space. This indicates that the presence of a network of interacting polymers in the condensates results in the R_g (Fig. S2, ESI†) and entropy (Fig. 2D) being less sensitive to temperature changes, even though some breakage of inter-actions occurs when the temperature approaches T_c (Fig. 2C). With the aid of time-resolved fluorescence spectroscopy, a recent study revealed extended conformation and enhanced conformational fluctuation for the tau protein (which is rich in positively charged amino acids) in the droplet phase, whereas it adopts a compact and less fluctuating globular state in the bulk.[22]

Translational diffusion of polymers in the dense phase

The high conformational entropies of the polymers in the condensates (Fig. 2D) together with their large number (Fig. 2C) of short-lived (Fig. S8, ESI†) intermolecular interac-tions are consistent with the liquid-like behavior of the dense phase. To quantify the liquid property, we measured the diffu-sion coefficients of the studied polyampholytes at a tempera-ture range that corresponds to 0.2–$0.9T_c$ of each system. The diffusion constants were evaluated by the slope of the linear fit to the mean squared displacement (MSD) of the polymers in the dense phase or in the bulk. MSD in three dimensions is related to the diffusion constant in the following way, $D = \dfrac{\langle (x(t) - x(0))^2 \rangle + \langle (y(t) - y(0))^2 \rangle + \langle (z(t) - z(0))^2 \rangle}{6t}$. When calculating the diffusion coefficient in the dense phase, we ensured that the polymers were part of the condensate for the entire time window we were interested in. Fig. 3A shows the ratio of the diffusion constant in the dense phase to that in bulk $\left(\dfrac{D_{Droplet}}{D_{Bulk}} \right)$, as a function of temperature scaled by T_c. Diffusion in the dense phase is 4–20 times slower than in the bulk, depending on T and κ. These diffusion coefficient values indicate pronounced diffusion within the droplet, which is consistent with earlier experimental measurements. For exam-ple, detailed solid-state NMR studies indicated that the ELP3 protein has a diffusion constant in the dense phase that is 10–100 times slower than in the bulk, depending on the salt concentration.[18] Also, HP1 protein diffuses 10 times more
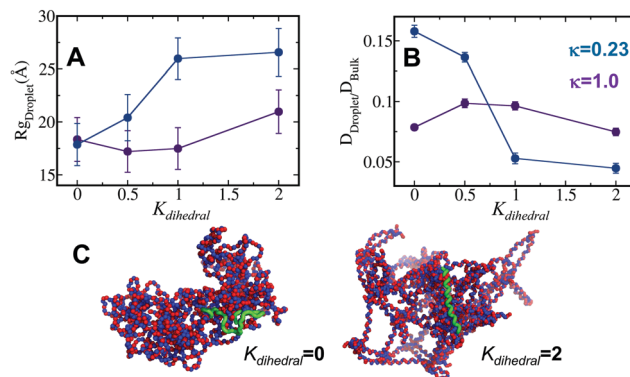

Fig. 4 Effect of polymers stiffness on structure and dynamics of the condensate. (A) The mean radius of gyration of individual polymers in the droplet can be affected by its rigidity. This effect was measured for peptides with $\kappa = 0.23$ (blue) or 1.00 (purple) at $T/T_c = 0.5$. (B) The diffusion coefficient relative to that in bulk is reduced for stiffer polyampholytes, particularly for those with low κ values. (C) Illustration of the condensate packing for $\kappa = 0.23$ and for flexible ($K_{dihedral} = 0$) and stiff ($K_{dihedral} = 2$) peptides. The peptides highlighted in green illustrate the conformation of a single peptide in the condensate and the increase in R_g shown in panel A.

slowly in the phase-separated compartments than in the nucleoplasm.[41]

For a specific κ value, the ratio $D_{Droplet}/D_{Bulk}$ strongly increases with increasing T (Fig. 3A). The increase in transla-tional diffusion in the dense phase with increasing T can be explained by the reduction of intermolecular interactions in the dense phase and their shorter lifetime at higher T (Fig. 2C and Fig. S9, ESI†). At a given T, the $D_{Droplet}/D_{Bulk}$ is larger for polyampholytes with smaller κ values (Fig. 3A, inset), again supported by their smaller number of intermolecular interac-tions (Fig. 2C, inset). It is worth noting that the slope of $D_{Droplet}/D_{Bulk}$ with respect to temperature also increases with decreas-ing κ, suggesting that the network of interactions in conden-sates formed for polymers of low κ is less dense and therefore more sensitive to temperature effects, consequently their diffu-sion coefficients tend to further increase with T. To illustrate pictorially the different characteristics of diffusion within con-densates formed by polyampholytes of different κ values, we followed the projection of the center of mass of three polymers in condensates of $\kappa = 1.0$ and $\kappa = 0.55$ at temperature $T = 0.5$ (Fig. 3B and C). The highlighted polymers are in close contact initially in both cases, but exhibit significant diffusion that is more extensive for $\kappa = 0.55$ than for $\kappa = 1.0$.

In addition to the effect of the charge pattern on the conformational preference of the peptides and their transla-tional diffusion in the droplet, the physical properties of the phase separated peptides may depend on their intrinsic flex-ibility. To address this aspect, we simulated droplet formation of polyampholytes with $\kappa = 0.23$ or 1.00 with three different degree of rigidity (introduced by $K_{dihedral} = 0.5$, 1.0, or 2.0). Introducing rigidity to the polyampholyte with $\kappa = 1$ has a minor affect, most likely because its charge pattern governs its rigidity even when there is no dihedral potential. As the rigidity increases for the peptide of $\kappa = 0.23$, it becomes more extended (*i.e.*, larger R_g) and its translational diffusion decreases about
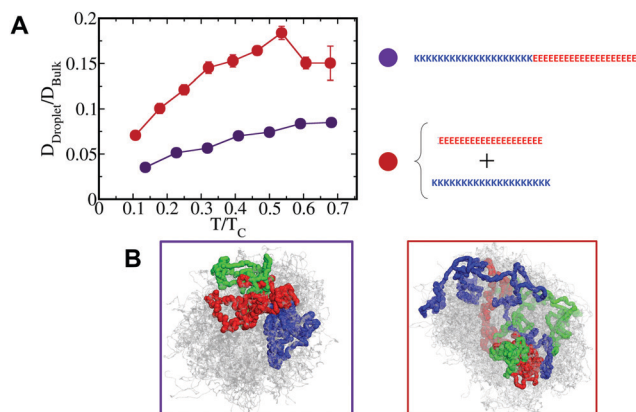
19372 | *Phys. Chem. Chem. Phys.*, 2020, **22**, 19368–19375

This journal is © the Owner Societies 2020

Fig. 5 Translational diffusion in the condensate of binary mixture. (A) The ratio of the translational diffusion coefficient (D) in the dense droplet phase to the bulk is shown as a function of temperature scaled to the critical temperature (T/T_c) for the binary mixture of 20-bead polymers with either positive or negative charges (brown). For comparison, the corresponding values for the 40-bead polymer with $\kappa = 1$ are shown (purple). (B) The effect of splitting the 40-bead polymer with $\kappa = 1$ into two 20-bead polymers on the diffusion in the dense phase is illustrated by projecting the center of mass of three selected chains (colored green, red, and blue) for 2000 timesteps (which correspond to $\sim$30 times the life time of an intermolecular contact), whereas the centers of mass of the other chains in the droplet are colored grey. The plots, made from a simulation sampled at $T = 0.9$, illustrate an enhanced diffusion in the condensate formed by the binary mixture (brown frame) compared to the condensate of the 40-bead polymer (purple frame).

3 folds. At high rigidity, the diffusion coefficient of the self-assembly of peptides with $\kappa = 0.23$ is not sensitive to temperature indicating a more solid-like assembly than a liquid droplet (Fig. 4).

The liquid properties of the condensate might be affected if the polyampholytes were fragmented.[42] To address this aspect, we studied a condensate formed by a binary mixture of the polyampholytes with $\kappa = 1$. In this case the 40-bead polymer was split into two halves: one with 20 positive charges and the other with 20 negative charges. The conformational and thermodynamic properties of the condensates formed by these two systems are similar. The main difference due to splitting the polymer with $\kappa = 1$ into two homogenously charged polymers is excessive dynamics in the latter reflected by $\sim$2-fold increase in the diffusion coefficient in the condensate. In the condensate formed by the 40-bead polymers with $\kappa = 1$, the intra-molecular interactions restrict exchange with neighboring peptides. This restriction is smaller in the condensate formed by the binary mixture of 20-bead polymers as all the attractive electrostatic interactions are intermolecular which results in enhanced diffusion (Fig. 5).

Shape anisotropy and lifetime of dense phase clusters

The effects of T and κ on the diffusion coefficients of polyampholytes in the dense phase indicate that the condensate may have a different viscosity from the bulk, with condensate viscosity potentially linked to the general shape of the condensate and the degree of its compactness. To quantify the geometry of the condensate, we calculated the shape anisotropy parameter, as defined below,

$$\text{Shape anisotropy}\,(p) = \max\left(\frac{d_x}{d_y}, \frac{d_y}{d_x}\right) + \max\left(\frac{d_y}{d_z}, \frac{d_z}{d_y}\right) + \max\left(\frac{d_x}{d_z}, \frac{d_z}{d_x}\right)$$
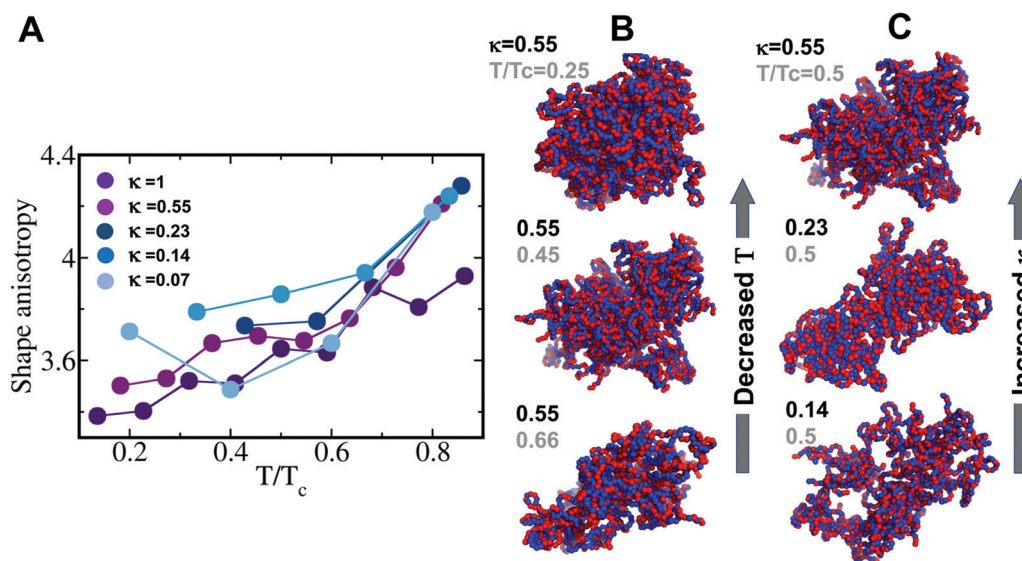

Fig. 6 Shape of the condensates. (A) Variation of the shape anisotropy parameter of the condensate with temperature for all the sequences. This analysis was performed for the largest condensate in the dense phase. A value of the shape anisotropy of 3 refers to an ideal sphere, with values > 3 referring to a more elongated shape. As temperature increases, the droplet becomes increasingly asymmetric and increasingly resembles a two-dimensional object with cavities within it. (B) Illustration of the shape of the largest cluster with decreasing scaled temperature for $\kappa = 0.55$. (C) Illustration of the shape of the largest cluster with increase in sequence κ at $T = 0.5T_c$. As temperature increases or as κ decreases, the droplet phase seems to become more elongated and to follow a transition from a 3D to a 2D shape. This transition is accompanied by the appearance of cavities within the droplet and by the presence of more chains on the droplet surface rather than at its core.

This journal is © the Owner Societies 2020

Phys. Chem. Chem. Phys., 2020, **22**, 19368–19375 | **19373**

where d_x, d_y and d_z denote the largest diameters of the largest cluster in the X, Y and Z dimensions, respectively. Following this measure, a spherically shaped condensate will be characterized by a shape anisotropy value of 3, while more elongated condensate shapes will acquire values larger than 3. A higher shape anisotropy value also indicates a shape that is more 2D than 3D. Fig. 6A shows shape anisotropy as a function of scaled temperature (*i.e.*, T/T_c) for the five polyampholytes with different κ values. For all systems, the shape anisotropy increases from 3.4 to 4.3, illustrating anisotropic expansion of the condensate. The effect of T on shape anisotropy is valid for all values of κ. We note that for $\kappa = 0.55$ or 1.0, a more spherical condensate shape is seen at low T, whereas for lower κ values, non-spherical shapes are seen even at low T. To illustrate pictorially the change in shape with κ and T, several snapshots are drawn that show the transition from sphericity to a more elongated shape as T increases and κ decreases (Fig. 6B and C, respectively). These snapshots illustrate that this transition to elongated and asymmetrical shapes is coupled with the appearance of cavities due to imperfect packing. Deviation from sphericity is also observed when the polyampholyets are stiff and adopt a more linear conformation, which restricts their packing and thus have many voids in the droplet phase (Fig. 4C).

Conclusions

In conclusion, this study captures the microscopic molecular features of liquid–liquid phase separation and the fascinating interplay of structure and dynamics in the dense phase. We observed a large-scale conformational unwinding of the polymers in the dense phase due to extensive intermolecular interactions with neighboring chains. Consequently, the polymers' dimensions obey the Flory theory for polymers in an ideal solvent. The liquid-like environment in the condensate is reflected in the polymers' high conformational entropy in the dense phase, which is higher than that in the bulk, so implying that conformal fluctuation is the key feature for the exchange of contacts in the dense network. Furthermore, translational diffusion in the condensate is just 4–20 times slower than that of isolated monomeric polymer in the bulk, in agreement with experimental studies.[18,25,41] Increased diffusion coefficients can be achieved for polyampholytes by either increasing the temperature or reducing the κ value by using smaller charge patches. Both scenarios result in fewer intermolecular interactions and thus less packed condensates that have a more elongated shape and may include cavities.

The appearance of cavities in the condensate, particularly for low κ values, can explain the oft-reported accumulation of water within droplets formed by LLPS.[43,44] Polyampholytes with lower κ values are also more likely to adopt a more elongated shape than a spherical one and this tendency increases with increasing temperature. We note that natural intrinsically disordered proteins have relatively low κ values in the range of 0–0.4.[36] Nevertheless, while some of the structural and dynamic properties presented here correlate with κ, others do not show a clear correlation, indicating the limitation of relying on the κ parameter[32] alone to capture entirely the biophysical properties of polyampholytes in the condensate. Our study highlights how the pattern of charges modulates the biophysics of LLPS *via* electrostatic interactions. Short-range hydrophobic interactions, which are prevalent is many intrinsically disordered proteins, should be examined in future to address the interplay between short- and long-range interactions in the liquid behavior of biomolecular condensates.

Conflicts of interest

There are no conflicts to declare.

Acknowledgements

References

1 C. P. Brangwynne, C. R. Eckmann, D. S. Courson, A. Rybarska, C. Hoege, J. Gharakhani, F. Julicher and A. A. Hyman, *Science*, 2009, **324**, 1729–1732.

2 C. P. Brangwynne, T. J. Mitchison and A. A. Hyman, *Proc. Natl. Acad. Sci. U. S. A.*, 2011, **108**, 4334–4339.

3 S. F. Banani, H. O. Lee, A. A. Hyman and M. K. Rosen, *Nat. Rev. Mol. Cell Biol.*, 2017, **18**, 285–298.

4 A. A. Hyman, C. A. Weber and F. Julicher, *Annu. Rev. Cell Dev. Biol.*, 2014, **30**, 39–58.

5 D. Hnisz, K. Shrinivas, R. A. Young, A. K. Chakraborty and P. A. Sharp, *Cell*, 2017, **169**, 13–23.

6 M. Morimoto and C. Boerkoel, *Biology*, 2013, **2**, 976–1033.

7 N. Kedersha, P. Ivanov and P. Anderson, *Trends Biochem. Sci.*, 2013, **38**, 494–506.

8 P. Anderson and N. Kedersha, *J. Cell Biol.*, 2006, **172**, 803–808.

9 P. Li, S. Banjade, H. C. Cheng, S. Kim, B. Chen, L. Guo, M. Llaguno, J. V. Hollingsworth, D. S. King, S. F. Banani, P. S. Russo, Q. X. Jiang, B. T. Nixon and M. K. Rosen, *Nature*, 2012, **483**, 336–340.

10 C. D. Reinkemeier, G. E. Girona and E. A. Lemke, *Science*, 2019, **363**(6434), eaaw2644.

11 E. W. Martin and T. Mittag, *American Chemical Society*, 2018, vol. 57, pp. 2478–2487.

12 J. M. Choi, F. Dar and R. V. Pappu, *PLoS Comput. Biol.*, 2019, **15**, e1007028.

13 J. M. Choi, A. Holehouse and R. Pappu, *Annu. Rev. Biophys.*, 2020, **49**, 107–133.

14 T. S. Harmon, A. S. Holehouse, M. K. Rosen and R. V. Pappu, *eLife*, 2017, **6**, e30294.

15 S. Elbaum-Garfinkle, Y. Kim, K. Szczepaniak, C. C. H. Chen, C. R. Eckmann, S. Myong and C. P. Brangwynne, *Proc. Natl. Acad. Sci. U. S. A.*, 2015, **112**, 7189–7194.

19374 | *Phys. Chem. Chem. Phys.*, 2020, **22**, 19368–19375

This journal is © the Owner Societies 2020

16 J. T. Wang, J. Smith, B. C. Chen, H. Schmidt, D. Rasoloson, A. Paix, B. G. Lambrus, D. Calidas, E. Betzig and G. Seydoux, *eLife*, 2014, **3**, e04591.

17 S. Elbaum-Garfinkle, Y. Kim, K. Szczepaniak, C. C. Chen, C. R. Eckmann, S. Myong and C. P. Brangwynne, *Proc. Natl. Acad. Sci. U. S. A.*, 2015, **112**, 7189–7194.

18 S. E. Reichheld, L. D. Muiznieks, F. W. Keeley and S. Sharpe, *Proc. Natl. Acad. Sci. U. S. A.*, 2017, **114**, E4408–E4415.

19 K. A. Burke, A. M. Janke, C. L. Rhine and N. L. Fawzi, *Mol. Cell*, 2015, **60**, 231–241.

20 V. H. Ryan, G. L. Dignon, G. H. Zerze, C. V. Chabata, R. Silva, A. E. Conicella, J. Amaya, K. A. Burke, J. Mittal and N. L. Fawzi, *Mol. Cell*, 2018, **69**(465-479), e467.

21 A. C. Murthy, G. L. Dignon, Y. Kan, G. H. Zerze, S. H. Parekh, J. Mittal and N. L. Fawzi, *Nat. Struct. Mol. Biol.*, 2019, **26**, 637.

22 A. Majumdar, P. Dogra, S. Maity and S. Mukhopadhyay, *J. Phys. Chem. Lett.*, 2019, **10**, 3929–3936.

23 I. Peran and T. Mittag, *Curr. Opin. Struct. Biol.*, 2020, **60**, 17–26.

24 C. W. Pak, M. Kosno, A. S. Holehouse, S. B. Padrick, A. Mittal, R. Ali, A. A. Yunus, D. R. Liu, R. V. Pappu and M. K. Rosen, *Mol. Cell*, 2016, **63**, 72–85.

25 J. P. Brady, P. J. Farber, A. Sekhar, Y. H. Lin, R. Huang, A. Bah, T. J. Nott, H. S. Chan, A. J. Baldwin, J. D. Forman-Kay and L. E. Kay, *Proc. Natl. Acad. Sci. U. S. A.*, 2017, E8194–E8203.

26 A. C. Murthy, G. L. Dignon, Y. Kan, G. H. Zerze, S. H. Parekh, J. Mittal and N. L. Fawzi, *Nat. Struct. Mol. Biol.*, 2019, **26**, 637–648.

27 E. W. Martin, A. S. Holehouse, I. Peran, M. Farag, J. J. Incicco, A. Bremer, C. R. Grace, A. Soranno, R. V. Pappu and T. Mittag, *Science*, 2020, **367**, 694–699.

28 G. L. Dignon, W. Zheng, R. B. Best, Y. C. Kim and J. Mittal, *Proc. Natl. Acad. Sci. U. S. A.*, 2018, **115**, 9929–9934.

29 G. L. Dignon, W. Zheng, Y. C. Kim, R. B. Best and J. Mittal, *PLoS Comput. Biol.*, 2018, **14**(1), e1005941.

30 G. L. Dignon, W. Zheng, Y. C. Kim and J. Mittal, *ACS Cent. Sci.*, 2019, 821–830.

31 J. McCarty, K. T. Delaney, S. P. O. Danielsen, G. H. Fredrickson and J. E. Shea, *J. Phys. Chem. Lett.*, 2019, **10**, 1644–1652.

32 S. Das, A. N. Amin, Y. H. Lin and H. S. Chan, *Phys. Chem. Chem. Phys.*, 2018, **20**, 28558–28574.

33 G. L. Dignon, W. W. Zheng and J. Mittal, *Curr. Opin. Chem. Eng.*, 2019, **23**, 92–98.

34 A. Statt, H. Casademunt, C. P. Brangwynne and A. Z. Panagiotopoulos, *J. Chem. Phys.*, 2020, **152**, 075101.

35 A. E. Conicella, G. L. Dignon, G. H. Zerze, H. B. Schmidt, A. M. D'Ordine, Y. C. Kim, R. Rohatgi, Y. M. Ayala, J. Mittal and N. L. Fawzi, *Proc. Natl. Acad. Sci. U. S. A.*, 2020, **117**, 5883–5894.

36 R. K. Das and R. V. Pappu, *Proc. Natl. Acad. Sci. U. S. A.*, 2013, **110**, 13392–13397.

37 Y. H. Lin, J. D. Forman-Kay and H. S. Chan, *Phys. Rev. Lett.*, 2016, **117**, 178101.

38 A. E. Conicella, G. Dignon, G. H. Zerze, B. Schmidt, A. M. D'Ordine, Y. Kim, R. Rohatgi, Y. M. Ayala, J. Mittal and N. L. Fawzi, *Biophys. J.*, 2020, **118**, 5A–6A.

39 M. T. Wei, S. Elbaum-Garfinkle, A. S. Holehouse, C. C. H. Chen, M. Feric, C. B. Arnold, R. D. Priestley, R. V. Pappu and C. P. Brangwynne, *Nat. Chem.*, 2017, **9**, 1118–1125.

40 A. Azia and Y. Levy, *J. Mol. Biol.*, 2009, **393**, 527–542.

41 A. R. Strom, A. V. Emelyanov, M. Mir, D. V. Fyodorov, X. Darzacq and G. H. Karpen, *Nature*, 2017, **547**, 241–245.

42 A. N. Amin, Y. H. Lin, S. Das and H. S. Chan, *J. Phys. Chem. B*, 2020, **124**, 6709–6720.

43 B. Y. Zaslavsky and V. N. Uversky, *Biochemistry*, 2018, **57**, 2437–2451.

44 S. S. Ribeiro, N. Samanta, S. Ebbinghaus and J. C. Marco, *Nat. Rev. Chem.*, 2019, **3**, 552–561.

This journal is © the Owner Societies 2020

Phys. Chem. Chem. Phys., 2020, **22**, 19368–19375 | **19375**